arXiv:1610.00337v2 [cond-mat.soft] 7 Oct 2016

Microfluidic Pumping by Micromolar Salt Concentrations

Ran Niu,[1] Patrick Kreissl,[2] Aidan T. Brown,[3] Georg Rempfer,[2] Denis Botin,[1] Christian Holm,[2] Thomas Palberg,[1] and Joost de Graaf[3,*]

[1]*Institut für Physik, Johannes Gutenberg Universität Mainz, 55128 Mainz, Germany*
[2]*Institute for Computational Physics, Universität Stuttgart, Allmandring 3, 70569 Stuttgart, Germany*
[3]*SUPA, School of Physics and Astronomy, The University of Edinburgh, King's Buildings, Peter Guthrie Tait Road, Edinburgh, EH9 3FD, United Kingdom*

(Dated: October 10, 2016)

A colloidal ion-exchange-resin-based microfluidic pump is introduced and experimentally characterized. It operates in almost deionized water for periods exceeding 24 h and effects fluid flows of $\mu m\,s^{-1}$ over hundreds of µm. This fluid flow displays a far-field, power-law decay which is characteristic of two-dimensional (2D) flow when the system is strongly confined in the vertical direction, and of three-dimensional (3D) flow when the system is less confined. Using theory and numerical calculations we show that our observations are consistent with electroosmotic pumping driven by $\mu mol\,L^{-1}$ ionic impurities in the sample cell, revealing the surprising impact of trace amounts of charge carriers. In addition, we explain how the power-law decay of the fluid flow can be understood on the basis of the confinement imposed by the sample cell. These two insights should benefit the design of a new class of microfluidic pumps.

I. INTRODUCTION

Fluid, solute, and colloid transport on the microscale pose a significant challenge, due to external pressure-driven pumping requiring the pump itself to withstand large forces. To circumvent this issue, a range of microfluidic pumps has recently been developed [1–21], most of which exploit self-generated solute gradients. Such pumps generate relatively small forces applied over a much larger range of the fluid through long-ranged concentration gradients. Typically, a solute-gradient-based pump consists of a source/sink of solute molecules, close to the surface of a sample cell. The solutes are produced/consumed either by chemical reactions on the surface of the pump [3–5, 9, 11–15, 17–21], the pump slowly dissolving [8], or exchange reactions taking place within the pump [16]. This sets up a concentration gradient in the fluid and along the surface of the sample cell. The interaction between the solutes and the surface causes a force on the fluid, which — coupled with the spatial heterogeneity of the solutes — leads to fluid flow, in a process that is referred to as osmosis [22]. Depending on the nature of the surface-solute interactions, neutral or Coulombic, the pump is either diffusioosmotic or electroosmotic. However, there is strong evidence that solute density [20] and thermal convection [18] effects also play a role for large pumps.

In this paper, we introduce and experimentally characterize an ion-exchange-resin pump. Our pump operates in almost completely deionized water for periods of over 24 h. We study the fluid flow by means of tracer velocimetry (close to the bottom of the sample cell) and show that the pumping speed is in the $\mu m\,s^{-1}$ range over hundreds of µm. We further demonstrate that the decay of the flow velocity can be modified by changing the geometry of the sample cell on the mm length scale. The far-field, power-law decay of the speed with the radial distance r is either quasi-2D ($\propto r^{-1}$) for small cell heights ($\leq 2\,mm$), or 3D ($\propto r^{-2}$) for tall cells ($\geq 10\,mm$). Even in the 2D regime, our system displays time-independent (steady-state) flow profiles. This is surprising, as 2D diffusive systems are not expected to exhibit steady-state solutions.

We interpret the experimental findings using a combination of numerical and analytic calculations. In our numerical work, we directly model the diffusion potential in the geometry of the experiment. We employ steady-state solutions for the concentration fields, electrostatic potential, and fluid velocity using the finite-element method (FEM). These computations go far beyond the thin electrostatic screening limit that is typically considered for such systems and give insight into the flow throughout the cell. Using analytic theory, we investigate the time-dependence of the flow in the quasi-2D far field.

Arguments are provided to show that the experimental observations can be understood by the resin exchanging trace amounts of cations from its surroundings with protons from its interior. We estimate the relevant trace cation concentration to be in the micromolar range. The pumping mechanism is electroosmosis: the difference in ion mobility between the protons and the exchanged cations sets up a diffusion potential that causes flow toward the exchange resin in the absence of a net electrical current. This mechanism is the same as that of similar ion-exchange pumps in saline solution [16].

Investigating the time-dependence of the result using analytic theory, we show that the experimentally observed steady-state flow is due to the flow being driven by concentration gradients. We further clarify the cause of the scaling with cell height. However, here we observe a lack of quantitative, but *not* of qualitative, agreement with the experiment. The power-law decay of the flow sets in unexpectedly close to the ion-exchange resin. We

*Electronic address: j.degraaf@ed.ac.uk

argue that this is due to ignoring solute transport by advection, which is necessary to make progress in both numerical and analytic theory. Studying the influence of advection by the fluid therefore presents challenges for future study.

Our results on ion-exchange pumps lead to the startling finding that trace amounts of ions released by the sample cell are sufficient to drive diffusion-potential electroosmosis. This insight should prove instrumental for the design of new microfluidic pumps operating in close-to-deionized water, and strongly indicates that the effect small amounts of charge and minute ionic fluxes may have significant consequences in other systems, such as chemically self-propelled colloids.

II. EXPERIMENTS

In this section, we describe the experimental setup for a single ion-exchange-resin pump and characterization of the tracer properties used in our velocimetry measurements. We also provide quantification of a wide range of resin pumps and tracers to show the generality of our findings. Finally, we study the impact of adding salt on the pumping.

A. Velocimetry for the Ion-Exchange-Resin Pump

Custom sample cells of radius $R = 10\,\mathrm{mm}$ and several heights H were constructed out of Poly(methyl methacrylate) (PMMA) rings attached to a microscopy glass slide and covered with another glass slide (soda lime glass of hydrolytic class 3 by VWR International), see the sketch in Fig. 1a. The glass slides were washed with alkaline solution (Hellmanex® III, Hellma Analytics) by sonication for 30 min, then rinsed with tap water, and finally washed several times with doubly distilled water (distilled using a quartz Hareaus Destamat; the conductivity was measured to be $55\,\mathrm{nS\,cm^{-1}}$). Spherical cationic resin beads (CGC50×8, Purolite Ltd, UK; exchange capacity $1.7\,\mathrm{eq\,L^{-1}}$ [39]) with radii ranging from 10 to 50 µm were carefully glued to the bottom glass slide with a tiny amount of two-component glue (UHU plus sofortfest, UHU GmbH, Germany), which was then set aside for 24 h to allow the glue to completely solidify. One resin bead was glued in each sample cell.

Polystyrene (PS) tracers were used for the velocity measurements. Stock PS particle suspensions (Microparticle GmbH, Germany) were diluted with distilled water and thoroughly deionized using ion exchange resin (Amberlite K306, Carl Roth GmbH + Co. KG, Karlsruhe, Germany). PS tracer electrophoretic mobilities were determined using micro-electrophoresis in a custom-built, disposable setup. We employed a Perspex cell 45 mm in height and with a square cross section (10 mm edge length). Based on the geometry of Uzgiris [23, 24] two platinum electrodes of width 1 mm were mounted into the center of the Teflon® cap sealing the cell. This ensures sufficient electrode-wall distances to effectively reduce stray-field-driven electroosmosis at the cell walls. Electrode spacing was set to 1 mm to obtain homogeneous electric fields and square wave alternating voltages of ±1 V were applied by a function generator (PeakTeck 4060 by PeakTeck GmbH, Germany). The cell was mounted on the stage of a micro-electrophoresis instrument (Mark II, Rank Bros. Bottisham, Cambridge, UK) supplying ultramicroscopic illumination and particle tracks were imaged using exposure times of 3 s on a consumer DSLR (D800, Nikon, Japan).

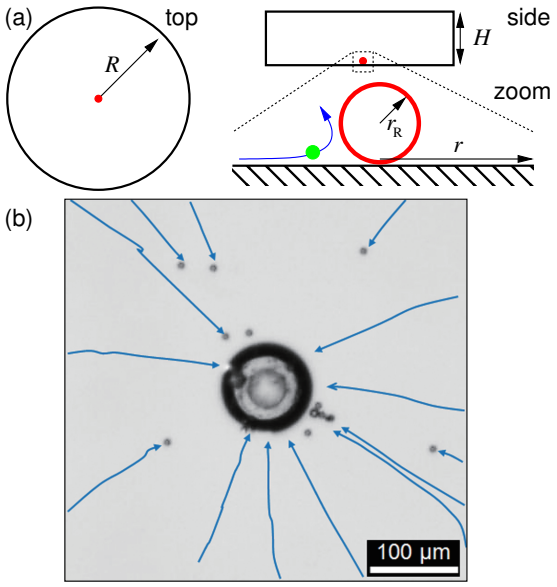

FIG. 1: The ion-exchange resin and sample cell. (a) Sketches of the geometry, showing top and side view of the cylindrical sample cell, with radius R and height H. A zoom-in shows the exchange resin, with radius r_R in red, a polystyrene (PS) tracer in green flowing along a blue flow line. In this paper, radial distance r is measured from the center of the resin. (b) Experimentally measured trajectories for the PS tracers (PS7) toward the resin (center of image), as shown in a top view microscopy image. Blue arrows indicate the paths of tracers, which are obtained from our image analysis.

TABLE I: The electrophoretic mobility μ_E of the PS tracer particles used in this work. The first column gives the label, the second the diameter, and the third the value of μ_E.

Type -	Diameter µm	μ_E $10^{-8}\,\mathrm{m^2\,V^{-1}\,s^{-1}}$
PS1	1.74 ± 0.04	-2.04 ± 0.19
PS7	7.57 ± 1.06	-2.56 ± 0.34
PS10	10.36 ± 0.87	-2.48 ± 0.32
PS15	15.17 ± 0.92	-2.54 ± 0.24
PS15COOH	15.47 ± 0.19	-2.12 ± 0.20

Electrophoresis was performed in the horizontal direction, while the particles sedimented in the vertical direction due to gravity. Thus the trace of a single particle has

a saw-tooth shape. The mobility of the particles $\mu_{\rm E}$ was calculated from the averaged velocity in the horizontal direction $v_{\rm E}$ and is given by: $\mu_{\rm E} = v_{\rm E}/E$. The obtained values of $\mu_{\rm E}$ are listed in Table I.

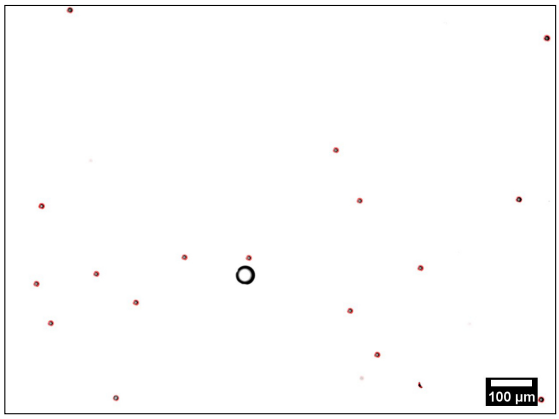

FIG. 2: Typical microscopy image of the tracers (red outlined circles) around the ion-exchange resin (black circle). The red outlines are obtained using the fit algorithm explained in the text.

The sample cell was loaded with a dilute PS tracer suspension, prepared according to the above deionization procedure. It was subsequently mounted on the stage of an inverted scientific microscope (DMIRBE, Leica, Germany), and observed in bright field, typically at 5× magnification. Images were shot with a DSLR and videos recorded with standard video equipment at frame sizes of 5.2Mpix and frame rates of 30fps. We imaged an area with cross-section of (typically) $\gg 1000\,\mu$m slightly above the bottom glass plate, focusing on the average hovering height of gravitationally settled PS tracers, see Fig. 2.

The resin bead glued to the glass slide displayed significant fluid pumping, as evidenced by the PS tracers moving toward the individual resin beads; Supplemental Movie "Exchange_Resin_Pump.avi" gives an example of this for tracers close to the resin. These tracers come in from far away, move up from the substrate close by, then away from the resin, sediment to the substrate, and finally move back toward the resin, leading to a recirculation of the tracer particles. Along their path the tracer speed varies as a function of r. The radial dependence of $U_{\rm PS}$ was determined from their positions in successive frames of the recorded movies. The positions of tracer particles were extracted using an in-house Python code. In brief: the circular perimeter of each particle was extracted using standard edge-detection methods, and then fitted to a circle using the Hough transform [25], implemented in the OpenCV function HoughCircle, see Fig. 2. Tracer positions in consecutive frames were compared to determine radial velocity. The velocity of a given tracer species at a given ion exchange-resin bead type was measured for $80-100$ individual PS particles for each bead and the results averaged over some $40-50$ beads.

We made use of the following expression to determine the tracer speed $U_{\rm PS}$

$$U_{\rm PS}(r) = \left\langle \frac{\hat{r}\cdot\Delta\vec{s}}{\Delta t} \right\rangle, \qquad (1)$$

where $\hat{r}$ is the 2D unit vector pointing from the resin to the tracer, $\Delta\vec{s}$ is the displacement of the tracer between frames (time between frames Δt), "$\cdot$" is the inner product, and $\langle\cdots\rangle$ indicates averaging over all tracers that are a distance r from the resin's center.

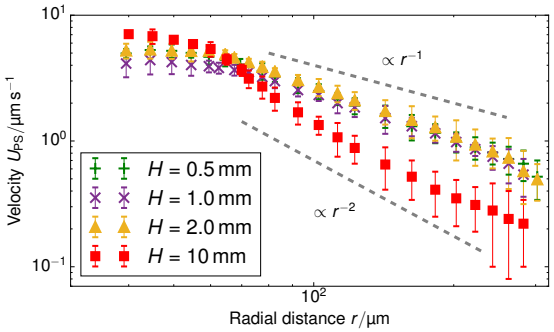

FIG. 3: The speed of the tracer $U_{\rm PS}$ as a function of the distance r for several values of the sample cell height H, an ion-exchange resin with radius $r_{\rm R} = 22.5\,\mu$m, and PS7 tracers. The symbols show the experimentally measured values; the standard error is given for each data point. The gray dashed lines serve as a guides to the eye for the power-law decay.

The results of our velocimetry are shown in Fig. 3, which provides $U_{\rm PS}$ as a function of their radial distance. Two regimes can be distinguished. For $r \lesssim 75\,\mu$m, there is a slight increase in the tracer speed, followed by a maximum and subsequent decrease (this is more evident in Fig. 4). For $r \gtrsim 75\,\mu$m the speed decreases with a power law and is appreciable over at least $300\,\mu$m. For sample cells with a height of $H = 1\,$mm, we find that $U_{\rm PS} \propto r^{-0.9\pm0.1}$ in the far field ($H = 0.5\,$mm, $U_{\rm PS} \propto r^{-1.2\pm0.1}$; $H = 2\,$mm, $U_{\rm PS} \propto r^{-1.1\pm0.1}$), while for the sample with height $H = 10\,$mm, the fitted decay is $U_{\rm PS} \propto r^{-2.2\pm0.3}$. We concentrate on understanding the far-field regime throughout this paper, as in the near field there are several competing effects, including electrophoresis, local flow, and interaction with the substrate, which complicate understanding of the physics in this regime.

B. Resin Size, Tracer Properties, and Salt Concentration

In this section we demonstrate the generality of the fluid pumping by ion-exchange resins. The systematic quantification of the tracer speed $U_{\rm PS}$ as a function of r is shown in Fig. 4.

- In Fig. 4a we vary the size of the PS tracers. In the far-field region there is a power-law decay of

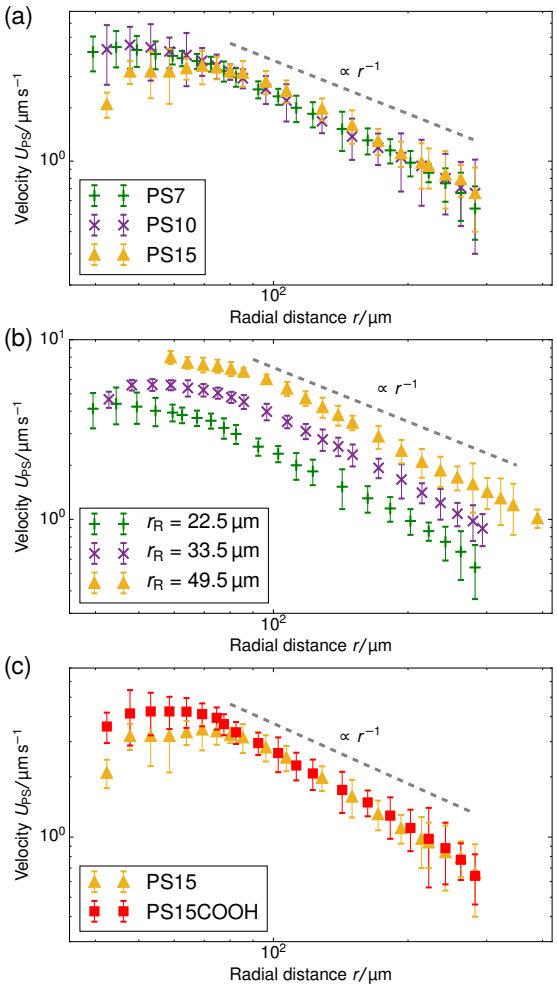

FIG. 4: Velocity of tracer particles $U_{\rm PS}$ as a function of radial distance r for a cell height of $H = 1.0\,$mm. (a) Three different sized PS particles are pumped by resin beads with $r_{\rm R} = 22.5\,\mu$m. (b) Three different sized resin beads are used to form a pump, the tracer particle is PS7 for each. (c) Two PS tracers of the same size, but with different $\mu_{\rm E}$, are pumped by resin beads with $r_{\rm R} = 22.5\,\mu$m. In all panels, the gray dashed line serves as a guide to the eye for the power-law decay and the standard error is given for each data point.

the tracer speed, which is insensitive to the type of tracer used within the error bar. Since the tracer's electrophoretic mobility is the same within the error bar, this shows that in the far-field the size of the tracer does not play a role.

- Figure 4b shows results for three resin sizes (radius $r_{\rm R}$). A larger resin induces a stronger electroosmotic flow over a larger range. We analyzed the far-field tracer speed by fitting the three curves using power-law decays. Then, we established the speed at the far-field distance ($r = 150\,\mu$m) as a function of the size. For these three data points, we found a linear dependence through the origin $U_{PS}(r = 150\,\mu\text{m}) \approx r_R(5.5 \pm 0.5) \times 10^{-2}\,\text{s}^{-1}$; the offset $\approx 0.15\,\mu\text{m}\,\text{s}^{-1}$ can be neglected — similar scaling was observed for other far-field distances. This strongly indicates that the process is diffusion limited. By the diffusion limit, we mean the upper speed limit imposed by the rate at which ions can diffuse towards the resin bead from the bulk reservoir. In this limit the flux through the particle surface $j_{s,\rm dl}$ (per unit area) is determined by the diffusivity of the ions $D^\star$ and the concentration far away $\rho^\star$, with the familiar diffusion-limit scaling $j_{s,\rm dl} \propto D^\star\rho^\star/r_{\rm R}$ [26]. The speed is proportional to the total flux through the resin, *i.e.*, $U_{\rm PS} \propto 4\pi r_{\rm R}^2 j_{s,\rm dl} \propto D^\star\rho^\star r_{\rm R}$, giving the linear dependence with $r_{\rm R}$ observed in the experiment.

- In Fig. 4c, we vary the electrophoretic mobility of the tracers, but not their size. It is evident that these tracer particles have the same velocity within the error bar in the power-law regime in spite of their mobilities differing by 25%; although $\mu_{\rm E}$ is comparable within the error bar. This again suggests that in the far-field regime the effect of tracer mobility is subdominant. In combination with our result for the size, this indicates that this regime is dominated by advection of the tracers by the fluid flow.

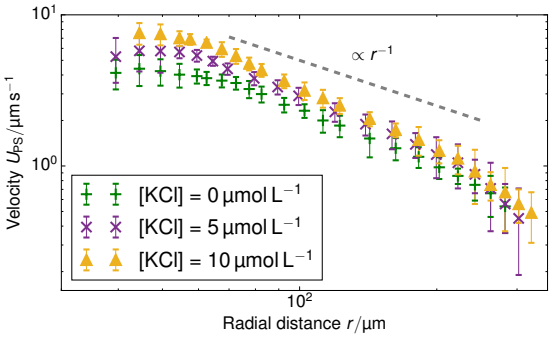

FIG. 5: Tracer speed $U_{\rm PS}$ as a function of radial distance r for different added KCl concentrations: no added salt (green plusses), 5 μmol L^{-1} (purple crosses) and 10 μmol L^{-1} (yellow triangles), for a cell with $H = 1.0\,$mm, resin with $r_{\rm R} = 22.5\,\mu$m. The gray dashed line serves as a guide to the eye for the power-law decay and the standard error is given for each data point.

Finally, we added KCl solution (Merck KGaA, Germany) to the sample cell for $H = 1\,$mm and the $r_{\rm R} = 22.5$ resin beads. Figure 5 shows the change in tracer speed: adding $5\,\mu\text{mol}\,\text{L}^{-1}$ KCl increases $U_{\rm PS}$, adding $10\,\mu\text{mol}\,\text{L}^{-1}$ instead, increases the speed further. That is, a higher concentration of exchangeable ions induces stronger flow. At a KCl concentration of $80\,\mu\text{mol}\,\text{L}^{-1}$, the velocity of tracer particles is effectively zero (therefore not shown here). For the $80\,\mu\text{mol}\,\text{L}^{-1}$ sample, we also do not observe any Brownian motion of the tracer beads. This indicates that the beads have become firmly

stuck to the sample cell wall, probably because of the increased electrostatic screening at this higher salt concentration. Therefore, we *cannot* use this data to infer a drop in pumping speed at higher salt concentration. This is in line with similar findings for chemically-propelled swimmers in Ref. [27].

C. An Inverted Pump

We inverted our setup to check whether solute density variations or thermal convection effects played a role in our system, as is the case in Refs. [18, 20]. That is, we glued the resin to the top glass slide and examined the movement of the tracers. In order to ensure that the tracers were at the top cover slide, we modified the overall density of the mixture by adding glycerol (water:glycerol mass ratio of 1:0.3) to slightly exceed the density of our PS particles. We used tracers with a diameter of 3.27 µm here and we increased the size of the ion-exchange resin to $r_R = 250\,\mu m$, in order to increase the speed of the tracers in this mixture of higher viscosity (approximately double that of water).

Supplemental movie "Inverted_Resin_Pump.avi" shows the result of this experiment. It is clear that inverting the pump did not change the direction in which the tracers move toward the resin. While we increased the overall density of the mixture, this should not affect the possible density variations induced by ion exchange. Our experiment therefore rules out density variation effects.

III. GENERAL CONSIDERATIONS

We performed a theoretical/numerical analysis of the pump to gain understanding of the fluid flow observed in our experiments. In this section, we start with several general considerations to provide a background for our calculations. (i) The resin is designed to exchange H^+ for other cations in the bulk, with a capacity of $1.7\,\mathrm{eq\,L^{-1}}$. There are *no* decomposition-type surface reactions. (ii) The surface of the sample cell is charged and we measured the zeta potential of the bottom glass slide to be $\zeta \approx -(105 \pm 5)$ mV [40]. The negative surface charge is due to the dissociation of surface groups, which release cations into the bulk. However, because the sample cell is filled with deionized water and carefully rinsed before preparation, there will be very few non-protonic cations present. (iii) Dissolved CO_2 forms carbonic acid and thus creates cations in the form of protons that screen the wall charge. We measured a pH ~ 5.4 at the onset of the experiment, consistent with typical pH values for water in equilibrium with atmospheric CO_2 [28]. The cations associated with CO_2 dissociation (protons) are the same as the ions inside the ion-exchange resin, so they cannot contribute to electroosmosis via ion exchange.

One might assume that the exchange resin cannot exchange protons for other cations, as any non-protonic cations released from the cell walls will have been washed away during preparation of the sample cell. This would then prevent diffusion-potential-based electroosmosis. This mechanism of generating fluid flow is as follows. Exchanged protons moving away from the resin have a higher mobility than the to-be-exchanged cations moving toward the resin — H^+ has the highest mobility of any ion — and thus a greater *diffusive* flux. To prevent bulk charge separation this self-generates an electric field (E-field) to compensate for the difference in diffusive flux with a migrative flux (*via* the E-field). The E-field points toward the resin and prevents charge separation in the bulk, by slowing down the H^+ and accelerating the cations, such that the total fluxes remain equal throughout. Since the associated electrostatic potential stems from a difference in ion diffusivity (equivalently mobility) the mechanism is "diffusion potential" based. The E-field acts on all ions in the system. However, there is a relatively high cationic concentration screening the negatively charged glass slides, resulting in net flow toward the resin, along the glass slides, and outward directed flow toward the center of the chamber, see Section VI, due to incompressibility of the fluid.

To determine if diffusion-potential-based electroosmosis is possible, we estimate the cation concentration that is required to fuel the pump. During a period of 24 h [41], a spherical pump of $r_R = 25\,\mu m$ in radius exchanges at most a part of its ionic content *via* an (assumed) constant surface flux density j_s. Let us further assume 25% of the original content to account for an unmodified pumping speed over the course of the experiment. Then it follows from the resin size and exchange capacity that $j_s \lesssim 5 \times 10^{-8}\,\mathrm{mol\,m^{-2}\,s^{-1}}$. This value is reasonable, as similar numbers are found for self-electrophoresing Janus swimmers that move at speeds comparable to our maximum U_{PS} [26]. To make this level of exchange possible, the non-protonic cation concentration in the sample cell has to be at least $1 \times 10^{-7}\,\mathrm{mol\,L^{-1}}$ — the total number of exchanged ions over 24 h and the volume of the sample cell were used to arrive at this number. Again, we can assume only a fraction of the total ions present are exchanged. This would lead to an estimate for the cation concentration of $\rho^\star = 1\,\mu\mathrm{mol\,L^{-1}}$ (if 10% is exchanged). Such low ion concentrations could be contributed by "impurity" cations released from the glass slides into the bulk fluid. Taking $\rho^\star$ and a typical value for cation diffusivity of $D^\star \approx 2 \times 10^{-9}\,\mathrm{m\,s^{-2}}$, the surface flux in the diffusion-limited regime is $j_{s,\mathrm{dl}} \approx D^\star \rho^\star / r_R = 4 \times 10^{-8}\,\mathrm{mol\,m^{-2}\,s^{-1}}$ (using K^+ for the cationic contaminant, which has a typical cation diffusivity). Our estimate for j_s is thus in the physically reasonable regime, close to the diffusion limit, in accordance with our experimental result.

We verified that this simple picture and our estimates can indeed give rise to the observed flow speed and direction using finite-element-method (FEM) simulations rep-

resentative of the experimental geometry, see Sections V and VI. We also used linearized, two-dimensional (2D) analytic theory to study the regime where the fluxes have become quasi-2D, *i.e.*, for $r > H$, see Section VII. In both cases, we solved the associated time-dependent electrokinetic equations, which we discuss next.

IV. ELECTROKINETIC EQUATIONS

To model the electroosmotic flow around the ion-exchange resin, we require three coupled equations, collectively known as the electrokinetic equations: Nernst-Planck for the solutes, Poisson for the electrostatics, and Stokes for the fluid flow, together with boundary conditions for the respective problems. We explain the three equations in detail below and discuss the boundary conditions for the simulations in Section V and the approximations made for the theory in Section VII, respectively.

The **Nernst-Planck equation** describes the diffusion and migration of the solute species. Here, we consider three ionic solute species in the fluid, protons H^+, potassium K^+, and chloride Cl^-. The protons are loaded in the exchange resin and the choice of the two ions is arbitrary. However, we picked two with almost equal diffusivities $D_{K^+} = D_{Cl^-}$ [29] to avoid the complication of additional (but relatively small) diffusion potentials. These three species are indexed by $i \in \{H^+, K^+, Cl^-\}$, respectively. We write ρ_i for the time- and space-dependent concentration fields and D_i for the molecular diffusivities. Then the flux of each species is given by

$$\vec{j}_i = -D_i \vec{\nabla} \rho_i + \vec{u} \rho_i - \frac{e z_i}{k_B T} D_i \rho_i \vec{\nabla} \Phi, \tag{2}$$

where $\vec{u}$ is the fluid velocity (accounting for advection), k_B is Boltzmann's constant, T the temperature, e the elementary charge, z_i the valency, Φ the electrostatic potential, and $\vec{\nabla}$ the gradient operator. The continuity equation is given by

$$\partial_t \rho_i = -\vec{\nabla} \cdot \vec{j}_i, \tag{3}$$

where ∂_t denotes the time derivative. For the steady-state problem $\partial_t \rho_i = 0$.

Before we move on to the other equations, we should comment on two simplifying assumptions typically made in the above description.

- We ignored the advective contribution to the flow in Eq. (2) in all our calculations. We consider the Péclet number, which give the ratio of diffusion to advection, to examine whether this is reasonable. A simple estimate is as follows: using a typical length scale of H for the development of fluid flow in this problem, a typical diffusivity of $D \approx 2.0 \times 10^{-9}\,\mathrm{m^2\,s^{-1}}$ [29], and a typical speed of $\bar{U}_{PS} \approx 1.0\,\mu\mathrm{m\,s^{-1}}$, we arrive at $\mathrm{Pe} = \bar{U}_{PS} H/D \approx 5$. This indicates that the value of Pe is likely high [42]. Our argument indicates that the Péclet number is not small in the experiment, therefore the advective term cannot be ignored in Eq. (2). However, due to the computational complexity of our FEM calculations, as well as the need to linearize our analytic theory, this approximation *must* be made in order to make progress. As we will see, the understanding of the physics of the resin pump is not strongly affected by this reduction.
- We have ignored bulk ionic association-dissociation reactions, as described in Ref. [26], which would have entered on the right-hand side of Eq. (3) as coupled chemical source and sink terms. In the physical system, bulk exchange will lead to coupling of the H^+ flux coming from the ion-exchange resin and H_2O and OH^- present in solution via $H_2O \rightleftharpoons H^+ + OH^-$ [43]. The main effect of these bulk reactions is to replace the relevant diffusion rate D_{H^+} with an effective rate

$$D_{av} \equiv \frac{D_{H^+} \rho^\infty_{H^+} + D_{OH^-} \rho^\infty_{OH^-}}{\rho^\infty_{H^+} + \rho^\infty_{OH^-}}, \tag{4}$$

  with ρ_i^∞ the concentration "very far" away from the resin [26]. For the experimental pH $\lesssim 5.4$, $[OH^-] \ll [H^+]$, so $D_{av} \approx D_{H^+}$, to within 2%. Hence, it is justified to ignore the bulk reactions here.

The electrostatic potential fulfills the **Poisson equation**, which is given by

$$-\epsilon_0 \epsilon_r \nabla^2 \Phi = \sum_i z_i \rho_i, \tag{5}$$

where ϵ_0 is the vacuum permittivity and ϵ_r the (spatially constant) relative permittivity. It should be noted that the ρ_i and Φ in the Poisson equation are time dependent and these two quantities provide the coupling between the Nernst-Planck and Poisson equations. For completeness, we introduce the electrostatic screening (Debye) length κ^{-1} here via

$$\kappa^2 = \frac{e^2}{\epsilon_0 \epsilon_r k_B T} \sum_i z_i^2 \rho_i^\infty. \tag{6}$$

Finally, we have the incompressible **Stokes equations** to describe the fluid flow. These read

$$\eta \nabla^2 \vec{u} = \vec{\nabla} p - \vec{f}; \tag{7}$$

$$\vec{\nabla} \cdot \vec{u} = 0, \tag{8}$$

with η the viscosity of the fluid, p the hydrostatic pressure, and $\vec{f}$ the body force. Here, $\vec{u}$ and $\vec{f}$ are time-dependent quantities. Given the electrostatic potential and the densities of all (charged) species, we can specify the body force on the fluid to close the problem as

$$\vec{f} = \sum_i \frac{k_B T}{D_i} \vec{j}_i. \tag{9}$$

This expression was obtained by first-order expansion of the chemical potential around thermodynamic equilibrium, which gives the gradient of the chemical potential as a driving force [30]. The specific choice of this driving force is to eliminate the spurious flow due to inexact cancellation of pressure and electrostatic interactions in FEM calculations. It is, however, completely equivalent [30] to the more commonly used expression

$$\vec{f} = \sum_i z_i e \rho_i \vec{\nabla}\Phi. \tag{10}$$

The only difference between Eqs. (9) and (10) is the interpretation of the hydrostatic pressure: Eq. (9) does not, while Eq. (10) does include the ideal-gas contribution from the dissolved solutes [30].

V. FINITE-ELEMENT MODEL OF THE PUMP

In this section we describe the boundary conditions for the above equation system and the specific choices made for the FEM modeling. Throughout, we used COMSOL Multiphysics Solver 5.2a to numerically solve the electrokinetic equations for a model setup of the experimental geometry.

We considered a cylindrical portion of the microscopy cell, with the resin located on the symmetry axis of the cylinder. Due to the rotational symmetry of this setup, the simulations could be performed on a quasi-2D axisymmetric domain, see Fig. 6. We considered two domains in order to simulate low sample heights $H \lesssim 1\,\mathrm{mm}$ (a) and high sample heights $H \gtrsim 2\,\mathrm{mm}$ (b) for the steady-state electrokinetic equations; we will come back to this in Section VI. The latter domain is a half-open domain, which we will refer to as "unbound".

Let us first describe the simulation domain that most accurately represents the experiment, see Fig. 6a. The bottom and top of the simulation domain correspond to the glass slides of the sample cell, the height of the sample cell H is fully resolved. The radius of the simulated geometry is R_{sim}. The spherical resin (experiment) is modeled as a hemisphere of radius r_{R} attached to the lower boundary (substrate). We chose a hemi-spherical resin, rather than a fully spherical one — as in the experiment — for simulation convenience. Specifically, the choice of a hemispherical resin facilitates the use of quadrilateral elements for the mesh, see inset to Fig. 7. This meshing would not be possible for a resin sphere in contact with the substrate, as is likely the case in the experiment, due to the cusp-like feature present in this geometry.

Quadrilateral elements are necessary, since we use the spurious-flow reducing method of Refs. [31–33]. This method consists of finely meshing several Debye lengths (in our case 6) using such elements around the walls and the rest of the domain using triangular elements, see Fig. 7. Quadrilaterals have the advantage that larger aspect ratios are permitted than for triangles, before numerical instabilities become important in FEM. It should

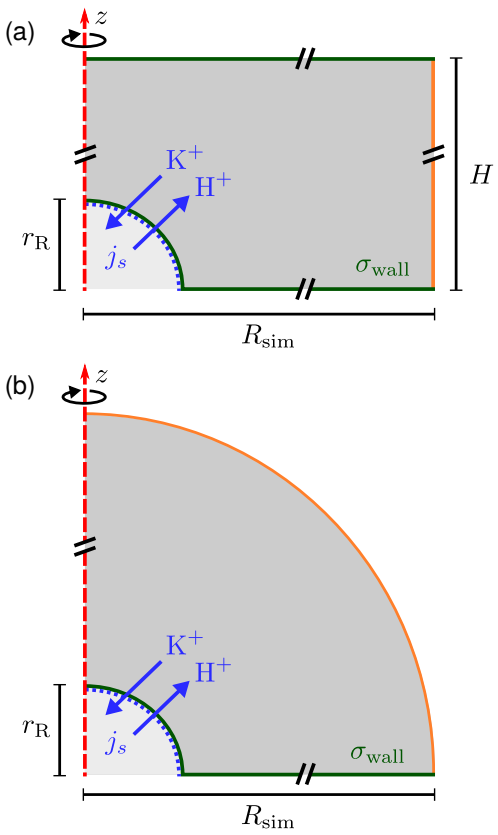

FIG. 6: Schematic of the rotationally symmetric (a) top-bound and (b) "unbound" simulation domain, the red dashed line shows the symmetry axis. The resin is modeled as a hemisphere of radius r_{R} (lower-left corner). Cation exchange is modeled by an inward/outward directed flux j_s of cations (K^+) and protons (H^+), respectively, see Eq. (12). A constant surface charge density σ_{wall} is imposed on the bottom (and top wall) and on the resin. All solid surfaces form no-slip boundaries for the hydrodynamics. The right-most boundary (orange line (a) or a circular arc (b)) is an "open boundary" for the hydrodynamic problem and we impose a pre-computed electrostatic profile and ion distributions on it, as explained in the text. Cut lines are used to emphasize that the domain is much larger than the resin, see Fig. 7.

be noted that our choice of a hemispherical resin will only affect the near-field flow around the resin. Beyond a certain distance, the resin can be considered a point source for protons and sink for potassium ions, respectively, and the details of its shape thus become irrelevant. This far field is the regime of interest to us.

At the edge of the domain, there is an "open boundary" for the hydrodynamic problem. This implies that there is no fluid momentum flux through the boundary. Since there is no convective momentum transport in the Stokes equations, there can be flow, but no stress normal to the boundary. This is a standard technique to model a piece of a domain that is embedded in a larger physical region, without modeling the full geometry, but allowing for the flow lines not to be closed within the domain. The

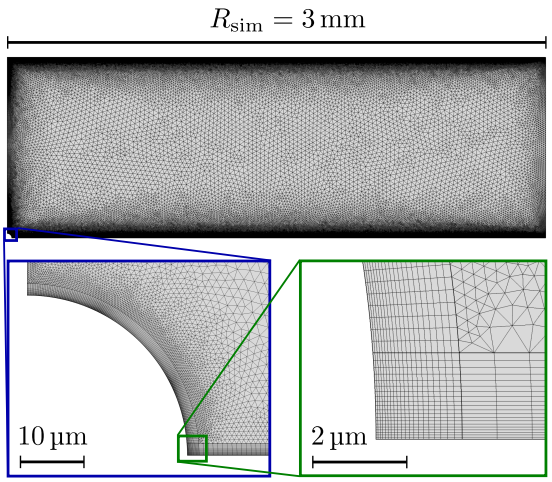

FIG. 7: Example of the finely resolved mesh used for our FEM calculations ($H = 1\,\mathrm{mm}$). Close to the electrically charged surfaces (within 6 Debye lengths) quadrilateral elements are used, see insets. The rest of the domain is composed of triangular mesh elements.

unbound simulation domain (Fig. 6b) is the same as the top-bound domain, but replaces the top glass slide with a hemispherical (open-boundary) domain.

We now provide the expressions for the boundary conditions used in the FEM model.

- For all solute species, no-penetration conditions are imposed in the **Nernst-Planck equation** on the bottom/top of the cell

$$j_s \equiv \hat{n} \cdot \vec{j}_i \Big|_{r_{\mathrm{R}}} = 0, \tag{11}$$

where $\hat{n}$ is the unit normal to the boundary pointing into the fluid.

For the resin, we only impose no-penetration conditions for Cl^-. The exchange of H^+ and K^+ is modeled via out- and influx on the resin, respectively. To be precise, we impose the following flux boundary condition

$$j_s \equiv \hat{n} \cdot \vec{j}_i \Big|_{r_{\mathrm{R}}} = \begin{cases} +k_{\mathrm{ex}}\rho_{\mathrm{K}^+} & i = \mathrm{H}^+ \\ -k_{\mathrm{ex}}\rho_{\mathrm{K}^+} & i = \mathrm{K}^+ \\ 0 & i = \mathrm{Cl}^- \end{cases}, \tag{12}$$

where k_{ex} is the ion-exchange rate coefficient, which we need to determine by fitting to the experimental data. Note that we have assumed that the exchange is determined entirely by the cation concentration close to the resin. This is probably valid as long as the H^+ concentration inside the resin is much larger than the cation concentration outside, which is the case for a fresh resin.

At the outer edge of the domain, the orange line in Fig. 6a, we impose concentration profiles for the ions that are based on the Poisson-Boltzmann solution for a two plate geometry with height H and surface charge σ_{wall}. For the geometry of Fig. 6b, the solution to the Poisson-Boltzmann equation for a single plate was used.

- For the **Poisson equation**, we impose a constant surface charge density σ_{wall} on all solid surfaces via

$$\hat{n} \cdot \vec{\nabla}\Phi = -\frac{\sigma_{\mathrm{wall}}}{\epsilon_0 \epsilon_{\mathrm{r}}}, \tag{13}$$

where the electrostatic potential is assumed to be evaluated at the boundary. The surface charge density is obtained from the experimental zeta-potential measurement through the Grahame equation [34]

$$\sigma_{\mathrm{wall}} = 2\epsilon_0\epsilon_{\mathrm{r}} k_{\mathrm{B}}T \sum_{i=0}^{2} \rho_i^{\infty} \left[\exp\left(-\frac{e z_i \zeta}{k_{\mathrm{B}}T}\right) - 1\right], \tag{14}$$

with ζ the zeta potential. Note that it is not clear what the most appropriate boundary conditions are for the resin surface, hence we chose the same boundary condition (Eq. (13)) as on the other surfaces for computational convenience.

- The boundary conditions for the incompressible **Stokes equation** are no-slip boundary conditions on all solid surfaces ($\vec{u} = 0$), that is the bottom and top of the cell, plus the resin. At the outer edge of the domain, a no-normal stress boundary condition is applied, which reads

$$\left[\eta\left(\vec{\nabla}\vec{u} + \left(\vec{\nabla}\vec{u}\right)^{\mathrm{T}}\right) - p\mathbb{I}\right] \cdot \hat{n} = 0, \tag{15}$$

with $^{\mathrm{T}}$ denoting transposition and $\mathbb{I}$ the identity matrix.

A final detail for the FEM solver is that we used polynomial ansatz functions of order 2 for the electrostatic, order 2 for the diffusion/migration, and order $3 + 2$ for hydrodynamic equations.

A. Tracer Speed

We determined the tracer speed from the solution of the above system of electrokinetic equations with boundary conditions as follows. The speed

$$U_{\mathrm{PS}} = \vec{u} \cdot \hat{r} + \mu_{\mathrm{E}} \vec{E} \cdot \hat{r}, \tag{16}$$

is comprised of an advective term, which is captured by $\vec{u}$, and a component deriving from the electrophoretic mobility $\mu_{\mathrm{E}}\vec{E}$. We evaluate the velocity and electric field at a constant "equilibrium height", $h^\star$, where gravity balances electrostatic repulsion from the wall. Throughout, we used a constant height of $h^\star = 5\,\mu\mathrm{m}$. The exact

height in the experiment is difficult to measure, presumably varies locally, and changes with the environment. We therefore varied $h^\star$ between 4 µm and 10 µm to check how our specific choice affected the result. The resulting speed profiles turned out to be virtually the same in this range. This is because the fluid flow velocity, which is the major component in the tracer speed, varies over a typical length scale of order $H \gg h^\star$. Note that Eq. (16) treats the tracer particle as if it were a point-like object, *i.e.*, it does not perturb the flow and electric fields by its presence.

B. Parameter Choices

We made the following parameter choices to simulate the experimental system. For the geometry of the simulation setup we typically chose: $r_\mathrm{R} = 25\,\mu\mathrm{m}$ for the radius of the resin and $R_\mathrm{sim} = 3\,\mathrm{mm}$ for the radius of the cylindrically symmetric domain. This choice was a compromise between the size of the sample cell, which is too large to numerically simulate in its entirety, and a domain size on which the power-law decay in the fluid velocity could be appreciated in the steady-state FEM calculations. The height of the domain was chosen to match the relevant experimental setup, *e.g.*, $H = 1\,\mathrm{mm}$, with the open simulation domain representing the $H = 10\,\mathrm{mm}$ domain, as we explain in Section VI.

The fluid represents water at room temperature ($T = 298.15\,\mathrm{K}$), which has a mass density of $\rho_\mathrm{f} = 1\times10^3\,\mathrm{kg\,m^{-3}}$, viscosity $\eta = 8.9\times10^{-4}\,\mathrm{Pa\,s}$, and relative permittivity $\epsilon_\mathrm{r} = 78.4$. The diffusivities of the ionic species are $D_{\mathrm{H^+}} = 9.3\times10^{-9}\,\mathrm{m^2\,s^{-1}}$ [35] and $D_{\mathrm{K^+}} = D_{\mathrm{Cl^-}} = 2.0\times10^{-9}\,\mathrm{m^2\,s^{-1}}$ [29]. The bulk concentration of impurities was chosen to be $\rho^\infty_{\mathrm{K^+}} = 1\,\mu\mathrm{mol\,L^{-1}}$, in line with our estimates from the experiment, and $\rho^\infty_{\mathrm{H^+}} = 0.1\,\mu\mathrm{mol\,L^{-1}}$ (pH = 7) or $\rho^\infty_{\mathrm{H^+}} = 4.0\,\mu\mathrm{mol\,L^{-1}}$ (pH = 5.4), with $\rho^\infty_{\mathrm{Cl^-}} = \rho^\infty_{\mathrm{K^+}} + \rho^\infty_{\mathrm{H^+}}$. The ion-exchange rate coefficient $k_\mathrm{ex} = 3.08\times10^{-6}\,\mathrm{m\,s^{-1}}$ was obtained by fitting the near-field velocity to the experiment for $H = 1\,\mathrm{mm}$ in Fig. 3. The surface charge density $\sigma_\mathrm{wall} = -4.03\times10^{-4}\,\mathrm{C\,m^{-2}}$ was computed from the experimentally measured zeta potential $\zeta \approx -0.1\,\mathrm{V}$ using Grahame's equation (14) [34].

VI. FINITE-ELEMENT RESULTS

The FEM-computed fluid flow for the steady-state problem is shown in Fig. 8 for a large portion of the sample cell; we used $H = 1\,\mathrm{mm}$. Both on the top and bottom wall the fluid flow is radially inward, due to the electroosmotic driving near the walls, with swirl-like patterns forming in the middle of the cell, due to the incompressibility of the fluid.

Fitting the near-field tracer speed U_PS for a cation concentration of $\rho = 1\,\mu\mathrm{mol\,L^{-1}}$ to the $H = 1\,\mathrm{mm}$ profile in

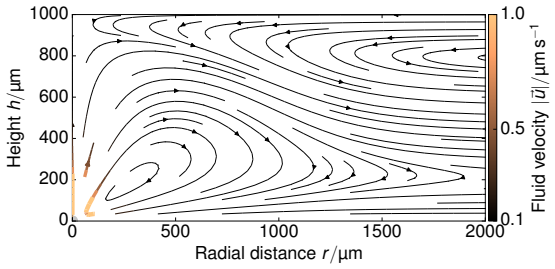

FIG. 8: Visualization of the FEM-calculated fluid flow in a $H = 1\,\mathrm{mm}$ sample cell over a radial range of 2 mm. The resin is shown in gray in the bottom-left corner, the direction of the fluid flow is shown with arrows, and color indicates the magnitude of the local velocity.

Fig. 3, we found that $k_\mathrm{ex} = 3.08\times10^{-6}\,\mathrm{m\,s^{-1}}$ is sufficient to match the experimentally observed near-field speed — compare Figs. 3 and 9a. We used this parameter throughout our simulations. This gives rise to an average surface flux of $j_s \approx 7\times10^{-8}\,\mathrm{mol\,m^{-2}\,s^{-1}}$, which corresponds closely to our back-of-the-envelope estimate in Section III.

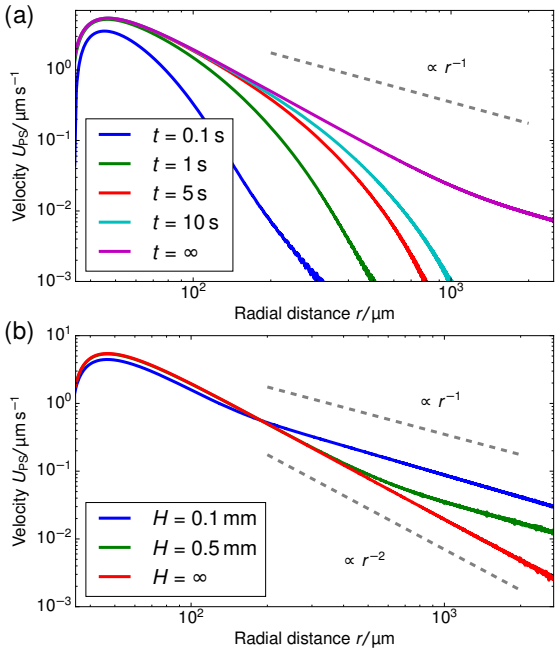

FIG. 9: The tracer speed U_PS obtained using our numerical calculations for several configurations of the system. (a) The time-dependent solution for U_PS as a function of the radial distance r for several times t, for PS7 tracers in a sample cell with height $H = 0.2\,\mathrm{mm}$. The steady-state solution is given by the purple curve ($t = \infty$). The power-law decay sets in only in to the far-right for long times. (b) The steady-state solution for several cell heights. The gray dashed lines serve as a guides to the eye for the power-law decay.

First, we verified that our steady-state solution for the quasi-2D domain gives a reasonable result, when com-

pared to the time-dependent simulations. We considered a cell height of $H = 0.2\,\mathrm{mm}$ for this problem, to avoid computational difficulties with simulation run time. Figure 9a shows several time-dependent tracer speed curves, up to the maximum time of $t = 10\,\mathrm{s}$ that we could access with our FEM calculations. Note that for these times, the long-time, far-field power-law decay has not yet set in. We estimate the time when the far-field, power-law decay sets in by the time it takes H^+ ions to diffuse a distance H: $t_{H^+} = H^2/D_{H^+} \approx 400\,\mathrm{s}$. This time is short on the time scale of the experiment, but too long to access *via* FEM calculations, which is why we consider analytic theory in Section VII. Nevertheless, the near-field solution has begun to converge to the steady-state after 10 s. Considering the relatively short time scales compared to the length of the experiment, on which convergence should take place, we are justified in neglecting of the time-dependence in the FEM calculations. To further probe the time dependence, we performed analytic calculations in Section VII for the far-field only.

Second, we considered the far-field r^{-1} scaling in our steady-state simulations in Fig. 9b. For increasing H there is an increasingly large intermediate range of 3D decay with r^{-2}. This is to be expected, because the minimum length (equivalently the time, in the time-dependent problem) that the ions travel before the quasi-2D decay sets in will increase with the height. This also explains the experimental observation of r^{-2} scaling for the $H = 10\,\mathrm{mm}$ sample cell in Fig. 3.

When solving the steady-state system of equations on the geometry of Fig. 6a, the flow field always decays with r^{-1} in the far field. This is because in the steady-state problem a sufficient amount of time has passed for the ions to "become aware" of their confinement, *i.e.*, stationarity is analogous to $t \to \infty$ in the time-dependent problem. Therefore, the experimentally obtained transition from quasi-2D to 3D decay by increasing the height H, cannot be observed in such a simulation. To observe a r^{-2} decay in the steady-state far field, an unbound domain must be simulated instead. Hence the need for the geometry of Fig. 6b.

Finally, comparing Figs. 3 and 9b, we find that the regime in which the power-law decay sets in is much closer to the resin in the experiment, *i.e.*, around 75 µm. This is counter intuitive, since on the basis of simple geometry arguments one would expect the ions to become aware of their 2D confinement when the distance they have diffused becomes comparable to the confining height. This suggests that there are mechanisms by which the ions are transported faster than through diffusion alone. A clear candidate is advection via the fluid flow, as the flow field around the resin, see Fig. 8, causes significant vertical displacement of the near-resin ions, provided the Péclet number is sufficiently large. We already estimated in Section IV that this is likely the case. Unfortunately, the effect of advection cannot be incorporated in this work due to numerical limitations, so that a quantitative match between theory and experiment is not possible. Nevertheless, the qualitative behavior that we do capture already provides important insight into the pumping mechanism.

VII. ANALYTICAL CALCULATIONS

In this section, we present an approximate, analytical solution to the electrokinetic equations on the domain of the sample cell. This allows us to obtain the time dependence and radial scaling of the flow in the far field. Our solution makes use of the equations provided in Section IV, where we already made the following simplifying assumptions: (i) Advection can be neglected. (ii) The only ions present are H^+, K^+, and Cl^-. (iii) The diffusivities of K^+ and Cl^- ions are equal. In order to make progress analytically, we also require: (iv) The perturbation of the ionic concentrations from their equilibrium distributions due to ionic fluxes generated by the resin bead are small compared to the background ionic concentrations — this is likely to be strictly valid only at short times or far from the central bead. (v) Far enough from the resin bead, the solution can be treated as 2D, and the bead as a point (δ-function) source. (vi) The electrostatic Debye screening length κ is much shorter than the relevant length scales of the problem, which is of order $\geq H$. (vii) The resin bead produces constant, equal and opposite fluxes of H^+ outwards and K^+ inward.

Under the above assumptions, we can combine Eqs. (2) and (3) to obtain

$$\partial_t x_{H^+} = D_{H^+}\nabla_{2D}^2\left(x_{H^+} + \psi\right) + \frac{\Gamma}{H\rho_{H^+}^{\infty}}\delta_{2D}(\vec{r}); \quad (17)$$

$$\partial_t x_{K^+} = D_{K^+}\nabla_{2D}^2\left(x_{K^+} + \psi\right) - \frac{\Gamma}{H\rho_{K^+}^{\infty}}\delta_{2D}(\vec{r}); \quad (18)$$

$$\partial_t x_{Cl^-} = D_{Cl^-}\nabla_{2D}^2\left(x_{Cl^-} - \psi\right), \quad (19)$$

where we define dimensionless concentrations $x_i \equiv (\rho_i - \rho_i^{\infty})/\rho_i^{\infty}$, the dimensionless electrostatic potential $\psi = \Phi e/(k_B T)$, and ∇_{2D}^2 is the 2D Laplacian. From the linear approximation (iv), we keep only terms up to linear order in x_i and ψ, and from the no-advection approximation (i), we neglect the term in $\vec{u}$. Here, the 2D radial vector $\vec{r} = \vec{x} + \vec{y}$ ($r = |\vec{r}|$) and δ_{2D} is the 2D δ-function, which is normalized so that $\iint \delta(\vec{r})\mathrm{d}^2\vec{r} = 1$, with the integral running over the whole plane. Γ is the total production rate of H^+ in molecules s^{-1}. Note that we do not make Γ dependent on ρ_{K^+}, as in the FEM model, to avoid complicating our calculation.

Linearizing the Poisson equation, Eq. (5) and defining the dimensionless background concentrations $\alpha_i \equiv \rho_i^{\infty}/(\sum_j \rho_j^{\infty} z_j^2)$ gives

$$\kappa^2 \sum_i \alpha_i z_i x_i = -\nabla_{2D}^2 \psi, \quad (20)$$

where the inverse Debye length κ is given by Eq. (6).

We now apply the thin-Debye-layer approximation (vi). Since we are interested in distances from the origin $r \gg H$, the capillary height, this approximation can be quantified as $\kappa r \gg 1$, and the approximation involves making an expansion to lowest order in the small parameter $1/(\kappa r)$. Now, from Eqs. (17)-(19), we must have that ψ and x_i are of similar order. However, if we multiply Eq. (20) by r^2, we see that the right-hand side is of order unity since $\nabla^2_{2D} = \mathcal{O}(r^{-2})$, but the left-hand side is of order $\kappa^2 r^2$. This means that, for consistency, the sum on the left-hand side of Eq. (20) must be zero to lowest order in $1/(\kappa r)$, *i.e.*,

$$\sum_i \alpha_i z_i x_i = 0 + \mathcal{O}\left((\kappa r)^{-2}\right). \tag{21}$$

That is, the charge density is approximately zero everywhere outside a thin Debye layer close to the capillary surface. Note that this does not mean that $\nabla^2_{2D}\psi = 0$, as from Eq. (20) it follows that the leading order term in $\nabla^2_{2D}\psi$ is equal to the finite next-to-leading-order term in the charge density. For simplicity, we write $\alpha_{H^+} = \alpha$ and, from the condition of charge balance in the background concentrations, $\alpha_{K^+} = 1/2 - \alpha$ and $\alpha_{Cl^-} = 1/2$. Then Eq. (21) can be rewritten as

$$2x_{H^+}\alpha + x_{K^+}(1-2\alpha) = x_{Cl^-}. \tag{22}$$

Equations (17)-(19) together with Eq. (22) represent a linear system of equations that we will now solve. From linear combinations of Eqs. (17)-(19), we can eliminate ψ, and Eq. (22) allows us to also eliminate x_{Cl^-}. This leaves us with two equations for x_{H^+} and x_{K^+}

$$\left(\frac{1}{D_{H^+}} + \frac{2\alpha}{D_{Cl^-}}\right)\partial_t x_{H^+} + \left(\frac{1-2\alpha}{D_{Cl^-}}\right)\partial_t x_{K^+} = \nabla^2_{2D}\left[(1+2\alpha)x_{H^+} + (1-2\alpha)x_{K^+}\right] + \frac{\Gamma}{H\rho^\infty_{H^+}D_{H^+}}\delta_{2D}(\vec{r}); \tag{23}$$

$$\left(\frac{2\alpha}{D_{Cl^-}}\right)\partial_t x_{H^+} + \left(\frac{1}{D_{K^+}} + \frac{1-2\alpha}{D_{Cl^-}}\right)\partial_t x_{K^+} = \nabla^2_{2D}\left[2\alpha x_{H^+} + 2(1-\alpha)x_{K^+}\right] - \frac{\Gamma}{H\rho^\infty_{K^+}D_{K^+}}\delta_{2D}(\vec{r}). \tag{24}$$

We solve these equations using the ansatz functions

$$x_{H^+} = \frac{\Gamma}{\rho^\infty_{H^+}H}\left[Af_1(r,t) + Bf_2(r,t)\right]; \tag{25}$$

$$x_{K^+} = \frac{\Gamma}{\rho^\infty_{K^+}H}\left[Cf_1(r,t) + Ef_2(r,t)\right], \tag{26}$$

where A, B, C, and E are constants, and $f_1(r,t)$ and $f_2(r,t)$ are given by the time-integral of the Green's function for the 2D diffusion equation [20], which accounts for the constant point-source at the origin

$$f_i = \int_0^t \frac{1}{4\pi\tilde{D}_i t'}\exp\left(\frac{-r^2}{4\tilde{D}_i t'}\right)\mathrm{d}t', \tag{27}$$

where the $\tilde{D}_i$, $i \in \{1,2\}$ are effective diffusivities to be determined. Directly solving for these effective diffusivities in general yields extremely unwieldy expressions, so instead we first make the simplifying assumption (iii) that $D_{K^+} = D_{Cl^-}$. This gives

$$\tilde{D}_1 = D_{K^+}; \tag{28}$$

$$\tilde{D}_2 = \frac{D_{H^+}D_{K^+}}{D_{K^+} + \alpha(D_{H^+} - D_{K^+})}, \tag{29}$$

We then solve for the constant terms in Eq. (26), yielding

$$A = 0; \tag{30}$$

$$B = 1; \tag{31}$$

$$C = \frac{1}{2(1-\alpha)}; \tag{32}$$

$$E = \frac{1-2\alpha}{2(1-\alpha)}. \tag{33}$$

Plugging these constants into Eqs. (25)-(26) and using $x_i \equiv (\rho_i - \rho_i^\infty)/\rho_i^\infty$ allows us to obtain the time-dependent ion density profiles. To calculate ψ, we take the time-derivative of Eq. (22), and using this to eliminate the left-hand side from Eqs. (17)-(19) obtain, after some algebra

$$\psi = -\frac{(D_{H^+} - D_{K^+})\alpha}{(D_{H^+} - D_{K^+})\alpha + D_{K^+}}x_{H^+}. \tag{34}$$

Using $\Phi = k_B T\psi/e$ this yields

$$\Phi = -\left(\frac{D_{H^+} - D_{K^+}}{D_{K^+}D_{H^+}}\right)\frac{e\Gamma}{4\pi\epsilon_r\epsilon_0 H\kappa^2}\int_0^t \frac{1}{t'}\exp\left(\frac{-r^2}{4\tilde{D}_2 t'}\right)\mathrm{d}t'. \tag{35}$$

The potential in Eq. (35) will generate an equal slip-velocity $\vec{u}_{slip} = (\zeta\epsilon/\eta)\vec{\nabla}_{2D}\Phi$ on both the upper and lower surfaces of the channel; we are sufficiently far away from the resin that the asymmetry caused by it being glued to

the bottom wall should not strongly affect the flow field. From Eq. (35) we then obtain

$$\vec{u}_{\mathrm{slip}} = -\frac{1}{r}\left[\left(\frac{D_{\mathrm{H}^+} - D_{\mathrm{K}^+}}{D_{\mathrm{K}^+} D_{\mathrm{H}^+}}\right)\frac{\zeta e \Gamma}{2\pi\kappa^2\eta H}\exp\left(\frac{-r^2}{4\tilde{D}_2 t}\right)\hat{r}\right]. \tag{36}$$

Strictly speaking, $\vec{u}_{\mathrm{slip}}$ is the velocity at the outer edge of the Debye layer. However, in the thin Debye limit, we can take $\vec{u}_{\mathrm{slip}}$ to be the fluid velocity on the wall itself. In the bulk of the channel, the fluid flow will vary with a typical length scale H, the capillary height. Therefore, we can use $\vec{u}_{\mathrm{slip}}$ as a good estimate for the velocity $\vec{u}_{\mathrm{PS}}(z)$ of a tracer particle located a small distance $z \ll H$ above the capillary surface, with a fractional error $\mathcal{O}(z/H) < 10^{-2}$ for the channels used here.

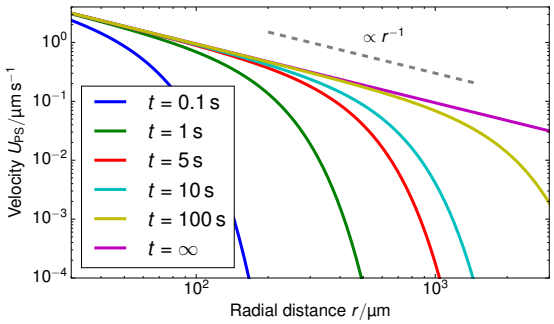

FIG. 10: The tracer speed U_{PS} obtained using our analytic theory as a function of the radial distance r for several times t, for PS7 tracers in a sample cell with height $H = 0.2\,\mathrm{mm}$, pH = 7, and $\Gamma = 2 \times 10^8\,\mathrm{s}^{-1}$; this models the setup of Fig. 9a. The steady-state solution is given by the purple curve ($t = \infty$). The gray dashed line serves as a guide to the eye for the power-law decay.

Figure 10 shows the tracer speed U_{PS} as a function of the distance as calculated using Eq. (36) for a sample cell with $H = 0.2\,\mathrm{mm}$ and other parameters the same as in Fig. 9a. Since the theory does not use the same expression for the surface fluxes (vii), we fitted the molecular exchange rate to give reasonable speed correspondence when compared to the results in Fig. 9a: $\Gamma = 2 \times 10^8\,\mathrm{s}^{-1}$. At long times, *i.e.*, for $t \gg r^2/\tilde{D}_2$, the exponential term approaches unity, so we obtain the $1/r$ scaling observed experimentally. At short times, the exponential term dominates.

Note that, as we would expect for a 2D system, the electrostatic field in Eq. (35) is not in steady state — the integral approaches $\log(t)$ in the limit of large t. Nevertheless, the flow field in Eq. (36) does approach a steady-state solution, see Fig. 10, because it scales with the gradient $\vec{\nabla}_{2\mathrm{D}}\phi$, which is in steady state.

The correspondence to the FEM calculations is semi-quantitative, despite the additional simplifying assumptions. However, it should be noted that we cannot make a prediction for the near-field using the theory, due to the quasi-2D assumption (v), nor do we account for advection of the solutes (i). This means that we cannot expect, nor do we find, quantitative agreement with the experiment.

VIII. CONCLUSION

In conclusion, we have introduced and experimentally characterized an ion-exchange-resin based microfluidic pump, which operates on $\mu\mathrm{mol\,L}^{-1}$ ionic concentrations for periods exceeding 24 h and produces pumping speeds of several $\mu\mathrm{m\,s}^{-1}$ over hundreds of μm. Using theory and simulations, we show that this pump operates via electroosmosis, by the exchange of cations for protons in its interior. The difference in ionic mobility between the cations and the protons for which they are exchanged sets up a diffusion potential that causes fluid flow directed toward the resin. We further showed that our pump's range can be tuned via the height of the sample cell to give either 3D or quasi-2D decay of the far-field flow velocity. Finally, we make a strong case in favor of including advective (fluid flow) contributions to the ionic fluxes in any future modeling of these systems, as these are likely the cause of the quantitative differences between the theory and experiment.

Our system showcases the significance of very small ionic concentrations and fluxes in microfluidic pumps and our results are highly suggestive that such fluxes may be responsible for flow and motion in a much wider range of out-of-equilibrium systems, such as for chemical swimmers and in biological processes.

Acknowledgements — JdG gratefully acknowledges financial support from a Marie Skłodowska-Curie Intra European Fellowship (G.A. No. 654916) within Horizon 2020. JdG and CH, as well as RN, DB, and TP, further thank the DFG for funding through the SPP 1726 "Microswimmers — From Single Particle Motion to Collective Behaviour" (HO1108/24-1 & Pa459/18-1).

[1] H. Andersson, W. Van Der Wijngaart, P. Nilsson, P. Enoksson, and G. Stemme, Sensors Actuat. B-Chem. **72**, 259 (2001).
[2] J. Santiago and D. Laser, J. Micromech. Microeng **14**, R35 (2004).
[3] T. Kline et al., J. Am. Chem. Soc. **127**, 17150 (2005).
[4] W. Paxton et al., J. Am. Chem. Soc. **128**, 14881 (2006).
[5] M. Ibele, Y. Wang, T. Kline, T. Mallouk, and A. Sen, J. Am. Chem. Soc. **129**, 7762 (2007).
[6] S. Chang, V. Paunov, D. Petsev, and O. Velev, Nat.

Mater. **6**, 235 (2007).
[7] A. Nisar, N. Afzulpurkar, B. Mahaisavariya, and A. Tuantranont, Sensors Actuat. B-Chem. **130**, 917 (2008).
[8] M. Ibele, T. Mallouk, and A. Sen, Angew. Chem. Int. Ed. **48**, 3308 (2009).
[9] I.-K. Jun and H. Hess, Adv. Mater. **22**, 4823 (2010).
[10] A. Shields et al., Proc. Nat.Ac. Sci. **107**, 15670 (2010).
[11] Y. Hong, M. Diaz, U. Córdova-Figueroa, and A. Sen, Adv. Funct. Mater. **20**, 1568 (2010).
[12] T. Hogg and R. Freitas, Nanomed.: Nanotech., Biol. and Med. **6**, 298 (2010).
[13] A. Solovev, S. Sanchez, Y. Mei, and O. Schmidt, Phys. Chem. Chem. Phys. **13**, 10131 (2011).
[14] H. Zhang et al., Angew. Chem. Int. Ed. **51**, 2400 (2012).
[15] V. Yadav, H. Zhang, R. Pavlick, and A. Sen, J. Am. Chem. Soc. **134**, 15688 (2012).
[16] A. Reinmüller et al., J. Chem. Phys. **136**, 164505 (2012).
[17] A. Farniya, M. Esplandiu, D. Reguera, and A. Bachtold, Phys. Rev. Lett. **111**, 168301 (2013).
[18] S. Sengupta et al., Nat. Chem. **6**, 415 (2014).
[19] M. Esplandiu, A. Afshar Farniya, and A. Bachtold, ACS Nano **9**, 11234 (2015).
[20] I. Ortiz-Rivera, H. Shum, A. Agrawal, A. Sen, and A. Balazs, Proc. Nat. Ac. Sci. **113**, 2585 (2016).
[21] C. Zhou, H. Zhang, Z. Li, and W. Wang, Lab on a Chip **16**, 1797 (2016).
[22] J. L. Anderson, Ann. Rev. Fluid Mech. **21**, 61 (1989).
[23] E. Uzgiris, Rev. Sci. Instr. **45**, 74 (1974).
[24] E. Uzgiris, Prog. Surf. Sci. **10**, 53 (1981).
[25] P. Hough, Machine analysis of bubble chamber pictures, in *International conference on high energy accelerators and instrumentation*, volume 73, 1959.
[26] A. Brown, W. Poon, C. Holm, and J. de Graaf, arXiv **1512.01778**, 1 (2016).
[27] A. Brown and W. Poon, Soft Matter **10**, 4016 (2014).
[28] F. Millero, Geochim. Cosmochim. Act. **59**, 661 (1995).
[29] H. Harned and R. Nuttall, J. Am. Chem. Soc. **71**, 1460 (1949).
[30] G. Rempfer, G. Davies, C. Holm, and J. de Graaf, J. Chem. Phys. **145**, 044901 (2016).
[31] G. Rempfer, S. Ehrhardt, C. Holm, and J. de Graaf, arXiv **1606.06432**, 1 (2016).
[32] G. Rempfer et al., Langmuir **32**, 8525 (2016).
[33] P. Kreissl, C. Holm, and J. de Graaf, J. Chem. Phys. **144**, 204902 (2016).
[34] D. Grahame, Chem. Rev. **41**, 441 (1947).
[35] W. M. Haynes, editor, *CRC handbook of chemistry and physics*, CRC press, Boca Raton, U.S.A., 93rd edition, 2013.
[36] T. Palberg et al., J. Phys.: Cond. Mat. **24**, 464109 (2012).
[37] Á. Delgado, F. González-Caballero, R. Hunter, L. Koopal, and J. Lyklema, J. Colloid Interface Sci. **309**, 194 (2007).
[38] U. Córdova-Figueroa and J. Brady, Phys. Rev. Lett. **100**, 158303 (2008).
[39] The eq stands for amount of charge that the resin can exchange (here per liter of resin): 1 eq = 1 mol of monovalent ions, 0.5 mol of divalent ions, etc.
[40] Doppler velocimetry with PS tracers [36], originally designed to measure bulk electrokinetics in colloidal suspensions, was here used to determine the electroosmotic mobility μ_{wall} of cleaned glass slides using a custom made cell with exchangeable sides for the top and bottom. Standard electrokinetic theory was used to calculate the zeta potential from the mobility [37].
[41] We experimentally measured a tracer speed decrease of only a factor 2 over a 24 h period, justifying the assumption of almost constant pumping.
[42] We believe that in practice the Pe number is likely to be self-limiting to a value $\approx$ 1, as found for chemically propelled swimmers [38]. This is because the high-concentration-gradient region centered around the colloid would be driven into the bulk of the channel by a strong advective current — see the direction of the flow lines in Fig. 8 — where it could no longer contribute to electrophoretic flow generation.
[43] There will be similar association-dissociation reactions involving dissolved CO_2 in water, as well as other species. The arguments provided here apply equally to these reactions.